Barriers to carrier transport in multiple quantum well nitride-based
c-plane green light emitting diodes

Cheyenne Lynsky [1,*] Abdullah I. Alhassan,[1,2,*] Guillaume Lheureux [1,*] Bastien Bonef [1] Steven P. DenBaars [1]
Shuji Nakamura,[1] Yuh-Renn Wu,[3] Claude Weisbuch,[1,4] and James S. Speck[1]

[1]*Materials Department, University of California, Santa Barbara, California 93106, USA*
[2]*National Center for Nanotechnology, King Abdulaziz City for Science and Technology (KACST), Riyadh 11442, Kingdom of Saudi Arabia*
[3]*Graduate Institute of Photonics and Optoelectronics and Department of Electrical Engineering, National Taiwan University,*
Taipei 10617, Taiwan
[4]*Laboratoire de Physique de la Matière Condensée, CNRS, IP Paris, Ecole Polytechnique, 91128 Palaiseau Cedex, France*

The presence of alloy disorder in III-nitride materials has been demonstrated to play a significant role in device performance through effects such as carrier localization and carrier transport. Relative to blue light emitting diodes (LEDs), these effects become more severe at green wavelengths. Because of the potential fluctuations that arise due to alloy disorder, full three-dimensional (3D) simulations are necessary to accurately relate materials properties to device performance. We demonstrate experimentally and through simulation that increased quantum well (QW) number in *c*-plane green LEDs contributes to excess driving voltage, and therefore reduced electrical efficiency. Experimentally, we grew an LED series with the number of QWs varying from one to seven and observed a systematic increase in voltage with the addition of each QW. Trends in LED electrical properties obtained from 3D simulations, which account for the effects of random alloy fluctuations, are in agreement with experimental data. Agreement is achieved without the need for adjusting polarization parameters from their known values. From these results, we propose that the polarization induced barriers at the GaN/InGaN (lower barrier/QW) interfaces and the sequential filling of QWs both contribute significantly to the excess forward voltage in multiple QW *c*-plane green LEDs.

I. INTRODUCTION

Group-III-nitride-based light emitting diodes (LEDs) are the attractive option for applications such as general illumination and display technologies as this materials system spans the full visible spectrum [1]. However, this advantage comes with well-known drawbacks, including the widespread growth of GaN on sapphire substrates that results in threading dislocation densities in excess of $10^8 \, \text{cm}^{-2}$ [2]. Coherently grown heterostructures, such as InGaN quantum wells (QWs) and GaN quantum barriers (QBs), in the *c*-axis [0001] orientation have large internal electric fields due to discontinuities in total polarization (sum of spontaneous and piezoelectric polarization) resulting from the 6mm symmetry of the wurtzite crystal structure [3]. Additionally, the large difference in band gaps of the constituent compounds (AlN, GaN, and InN) results in significant spatial variations in the band energy of their alloys (AlGaN and InGaN) [4] as well as large conduction and valence band offsets in heterostructures. Both the energy band fluctuations resulting from alloy fluctuations and the large band offsets directly impact carrier localization and transport. The presence of alloy disorder in the III-nitrides materials system necessitates the use of full three-dimensional (3D) simulations to accurately capture carrier behavior and achieve simulations that are consistent with experimental observations [4,5].

Long-wavelength LEDs are achieved by increasing the indium content in the InGaN QWs, which has several deleterious effects on the internal quantum efficiency (IQE). The IQE of an LED is given by the ratio of the radiative recombination rate to the recombination rate of all processes (radiative and nonradiative). Some of these effects are related to the increased alloy fluctuations, while some are not. To increase indium incorporation, InGaN QWs are grown at lower temperatures, leading to materials degradation and a higher Shockley-Read-Hall (SRH) nonradiative recombination rate An (where A is the SRH coefficient and n is the carrier density) [6,7]. Additionally, the polarization discontinuity at the QW and barrier interface becomes larger as the In fraction of the InGaN QW is increased. The resulting electric fields in the QW spatially separate electron and hole wave functions, thereby reducing their overlap and the bimolecular radiative recombination rate Bn^2 (where B is the radiative recombination coefficient). Last, increased alloy fluctuations in high In fraction QWs lead to stronger carrier localization and a higher Auger nonradiative recombination rate Cn^3 (where C is the band-to-band Auger recombination coefficient) [4]. The reduced wave-function overlap in high In content QWs also leads to higher overall carrier densities, thereby increasing Auger recombination at a given current density [8,9].

---

*These authors contributed equally to this work.

In addition to a lower IQE, state-of-the-art long-wavelength LEDs operate with significant excess forward voltage and therefore low electrical efficiency (EE). The forward voltage V_F is prescribed at a specific current density, such as $20\,\mathrm{A\,cm^{-2}}$, and ideally V_F is approximately equal to the photon voltage V_{ph}, where $eV_{ph} = h\nu$. Compared to blue LEDs, typical green LEDs suffer from poor power conversion efficiency (PCE) in part due to their large excess forward voltage ΔV_F, where $\Delta V_F = V_F - V_{ph}$ [10–12]. The EE is related to the photon voltage and forward voltage, where $\mathrm{EE} = V_{ph}/V_F$. The PCE can then be described in terms of IQE, EE, and light extraction efficiency (LEE) by the following equation: $\mathrm{PCE} = \mathrm{EE} \times \mathrm{IQE} \times \mathrm{LEE}$. From this equation, it is seen that V_F and IQE play an equal role in the overall device PCE. While numerous publications focus on understanding the low IQE of green LEDs [6–8,13,14], significantly less research has been devoted to identifying the barriers to carrier transport that lead to their low electrical efficiency [15–17]. The purpose of the present paper is to identify the impact of large band discontinuities and internal electric fields on excess forward voltage in multiple QW (MQW) green LEDs.

The role of QW number on LED device performance has been explored in several previous publications. In an early report, Chang *et al.* measured an increase in V_F with QW number in blue and green LEDs, which they partially attributed to an increase in series resistance and partially to the built-in voltage of the entire heterostructure [15]. Relative to the blue LED devices, they observed higher V_F in the green LEDs, which they ascribed to a higher resistivity of the green LED active region resulting from lower growth temperature. Xia *et al.* simulated an increase in V_F with higher QW number in blue LEDs, which they also attributed to an increase in series resistance [16]. Chang *et al.* performed simulations on blue LEDs with either InGaN or GaN QBs and one or five QWs [17]. They explained the lower voltage in InGaN barrier LEDs by reduced polarization-induced triangular barriers. They also concluded that the number of triangular barriers (number of QWs) influences electrical properties. As we will show below, the addition of QWs should not change the built-in voltage of the diode and the polarization-related barriers cannot be described as the addition of a simple series resistance.

Using here the combined experimental results and a computational approach based on landscape theory of disorder [5,18,19], we demonstrate why the number of QWs has a significant impact on V_F in c-plane green LEDs. We grew samples with a varying number of QWs using metalorganic chemical vapor deposition (MOCVD) and performed 3D simulations of the structures. We measured, on average, an additional voltage per quantum well (hereafter called the voltage penalty) of $0.41\,\mathrm{V}$ at $100\,\mathrm{A\,cm^{-2}}$, similar to the penalty predicted by 3D simulations. These data support prior results which demonstrated that polarization discontinuities at the heterointerfaces, mostly due to strain-induced (piezoelectric) polarization resulting from lattice mismatch between InGaN and GaN, act as barriers to efficient carrier transport in unipolar MQW structures [20]. Therefore, additional bias must be applied to overcome the polarization-induced barriers and allow carriers to surmount the barriers to reach the QW. From 3D simulations, we observe that sequential injection of the QWs also contributes to the high V_F in these structures.

Our findings indicate that careful design of the active region is essential to avoid excess voltage in multiple QW green LEDs.

II. EXPERIMENT

Green LEDs with a varying number of QWs (one, two, three, five, and seven QWs) were grown by atmospheric pressure MOCVD on (0001) patterned sapphire substrates (PSSs). A low-temperature GaN nucleation layer was followed by a 3-μm high-temperature unintentionally doped (UID) GaN layer, a 2-μm Si-doped n-GaN layer ($[\mathrm{Si}] = 6 \times 10^{18}\,\mathrm{cm^{-3}}$), a ten-period n-$\mathrm{In_{0.05}Ga_{0.95}N}$ (3 nm)/GaN (5 nm) superlattice layer ($[\mathrm{Si}] = 6 \times 10^{18}\,\mathrm{cm^{-3}}$), and an 8-nm UID GaN layer. Next, the active region was grown undoped and consisted of 3-nm $\mathrm{In_{0.22}Ga_{0.78}N}$ QWs, 2-nm $\mathrm{Al_{0.20}Ga_{0.80}N}$ capping layers, and 8-nm GaN barriers. The active region was followed by 25 nm of highly doped p-GaN ($[\mathrm{Mg}] = 1.5 \times 10^{20}\,\mathrm{cm^{-3}}$), 90 nm of p-GaN ($[\mathrm{Mg}] = 3 \times 10^{19}\,\mathrm{cm^{-3}}$), and a 10-nm highly doped p-GaN contact layer. The active region design of these LEDs was optimized in previous work to improve the green LED power and external quantum efficiency [21–23]. The use of an AlGaN capping layer after the QW allows for aggressive growth conditions in the quantum barriers, such as high-temperature GaN growth and the introduction of $\mathrm{H_2}$ carrier gas. All samples were grown to minimize V-defect formation and thus the electron and hole injection into the QWs is through the c-plane interface [10–12].

All samples underwent a postgrowth anneal in $\mathrm{N_2/O_2}$ at $600\,^\circ\mathrm{C}$ for 15 min to activate the Mg-doped layers. The samples were then fabricated into LEDs using standard mesa isolation and contact deposition. Pd/Au was used as the contact to p-GaN for simple fabrication and reliable voltage determination. The device area was taken to be the area of the contact pad deposited on the mesa, where the contact pad area was 90% that of the mesa area.

Simulations of the optical and electrical properties of green LEDs require prior knowledge of the composition and thickness of the InGaN and AlGaN layers comprising the active region [5]. Detailed layer thicknesses and composition information can be obtained using atom probe tomography (APT) [24–26]. Here, the five-QW sample was investigated. Details of the APT sample preparation, evaporation, and reconstruction parameters can be found in [25].

Figure 1(a) shows the APT reconstruction of the five-QW sample. The five InGaN/AlGaN/GaN QWs/cap layers/QBs can be clearly observed in the figure. Figure 1(b) is a 1D concentration profile showing the In and Al III-site fraction variations in the active layer along the [0001] direction. The peak In fractions measured in the different InGaN QWs are 0.22 ± 0.02, 0.22 ± 0.02, 0.23 ± 0.02, 0.22 ± 0.02, and 0.22 ± 0.02 from the bottom to the top of the structure, which indicates well-controlled growth of the InGaN layers. The average Al composition in the capping layers was ~ 0.20, which is consistent with the composition expected from growth calibrations. Despite the inability of APT to resolve atomic planes in the [0001] direction in group-III-N materials [27,28], the thickness of QWs can be estimated from the concentration profile in Fig. 1(b). The full width at half maximum (FWHM) of the In profiles are used to measure the QW thicknesses. From the bottom to the top of the structure,
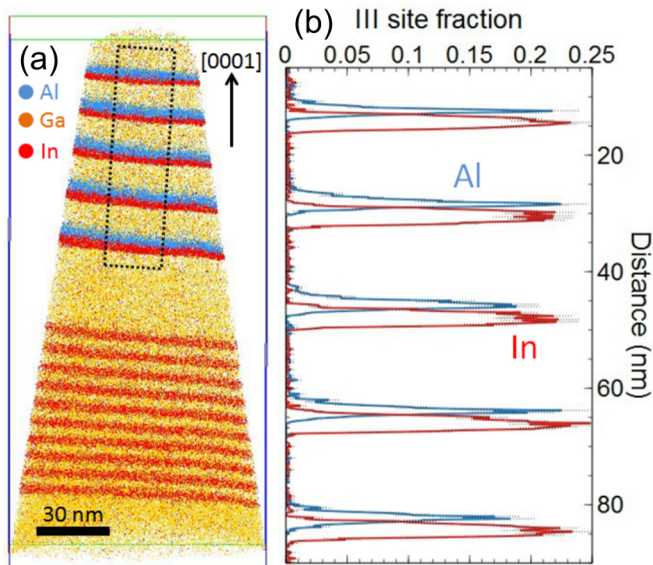
FIG. 1. (a) APT 3D reconstruction of the active region for the five-QW sample. The InGaN/GaN superlattice and the five-period InGaN/AlGaN/GaN QWs/cap layers/QBs can be observed in the reconstruction. (b) 1D concentration profile of In and Al measured along the [0001] direction and in the region defined in (a).

the measured thicknesses are 2.8, 2.9, 2.9, 3, and 2.8 nm, which again closely agrees with values predicted from InGaN growth rate calibrations.

Finally, statistical distribution analyses (SDAs) were performed on the InGaN QWs to investigate their respective alloy distributions [29]. The experimental alloy distribution measured by APT are compared to the binomial distribution expected for random alloys, as described in [24] and [30]. SDA revealed that the five-QW alloy compositions are randomly distributed in the QW plane, as usually observed for *c*-plane InGaN [31,32]. The results from APT are therefore reliable inputs for device simulations.

Rational heterostructure design via realistic 3D simulations is central to realizing reduced V_F. The random alloys in the active region of LEDs, such as InGaN and AlGaN, have intrinsic compositional fluctuations which translate into potential fluctuations. These in turn give rise to local potential barriers and minima that directly impact carrier localization, transport, and recombination. A fine mesh (∼0.2–1 nm) is required to correctly capture the physical scale of these phenomena. In addition, the 3D simulations must self-consistently account for the carrier-induced modifications of internal potentials and the changing 3D potential over a wide range of diode biases and injected currents. A Schrödinger-Poisson drift-diffusion solver should be used to calculate energy levels, density of states, and transport properties under such circumstances. However, this presents a nearly impossible task as the number of mesh nodes exceeds ∼10^6 [5]. To capture the inherent 3D nature of nitride LEDs, the 3D drift-diffusion charge control (3D-DDCC) solver [33] is used to simulate the electrical behavior of semiconductor devices by self-consistently solving the Poisson, landscape, and drift-diffusion equations in 3D structures. In this 3D-DDCC solver, the Schrödinger equation

is replaced by the landscape equation [18,19]:

$$\left(-\frac{\hbar^2}{2m_{e,h}^*}\Delta + E_{c,v} \right)u_{e,h} = 1,$$

where $m_{e,h}^*$ is the effective mass of the electron/hole, $E_{c,v}$ is the conduction/valence band energy, and $u_{e,h}$ is the landscape function for the electron/hole. The landscape equation is used to predict the energy levels and local density of states (LDOS) in place of the Schrödinger equation. The quantity $1/u_{e,h}$ is interpreted as the effective potential for the carrier, accounting for their quantum nature and particular behavior, such as confinement in a quantum well [18]. Thus, $1/u_{e,h}$ is used directly to plot an effective band diagram for a given structure. The use of the landscape equation in lieu of Schrödinger's equation leads to a 10^3 decrease in computation time [5], thus making 3D self-consistent computations possible.

The 3D-DDCC solver is based on a finite element method (FEM) computational approach; the complete description of the method and parameters used can be found in [34]. All simulations presented here use 100% of the known values for the spontaneous and piezoelectric polarization parameters [3]. The green LED structure was first defined by specifying the thickness, doping, and carrier lifetimes of the different layers. The simulated structures were similar to the experimental structures described above, with the exceptions of thinner *p*-GaN and *n*-GaN layers of 40 nm and exclusion of the superlattice to limit the number of mesh points. The differences between the simulated and experimental structures do not impact the final results. The active region was composed of $n \times 3$ nm In$_{0.22}$Ga$_{0.78}$N QWs, $n \times 2$ nm Al$_{0.20}$Ga$_{0.80}$N cap layers, and $(n+1) \times 8$ nm GaN barriers, where n is the number of QWs. The lateral dimension of the domain was 30 nm × 30 nm and Born–Von Karman boundary conditions were applied such that the simulated system behaves as a semi-infinite medium. The domain was then meshed into small elements using gmsh [35]. The mesh size was refined around the alloy regions of the structure (InGaN QWs and AlGaN cap layers). The mesh size in the *XY* lateral dimension was 0.5 nm × 0.5 nm and ranges between 0.2 and 1 nm in the *Z* direction. Finally, the alloy composition map was randomly generated using a Gaussian average weight method and affected to the node of the mesh. The strain and polarization fields (spontaneous and piezoelectric) were calculated before entering the self-consistency loop [5].

1D simulations were also performed for comparison with experiment and 3D simulations. The 1D drift-diffusion charge control (1D-DDCC) solver was used, which is based on the landscape equation [18,19,33] and assumes 100% polarization fields. These 1D simulations cannot account for in-plane alloy fluctuations. The InGaN QW and AlGaN cap concentration profiles in the *Z* direction are described by step functions, rather than the Gaussian profiles used in 3D simulations.

III. RESULTS AND DISCUSSION

Experimental current density-voltage (*J-V*) characteristics of the LEDs are shown as solid curves in Fig. 2; for a given current density, an increase in V_F is observed with increasing number of QWs. The peak electroluminescence wavelength
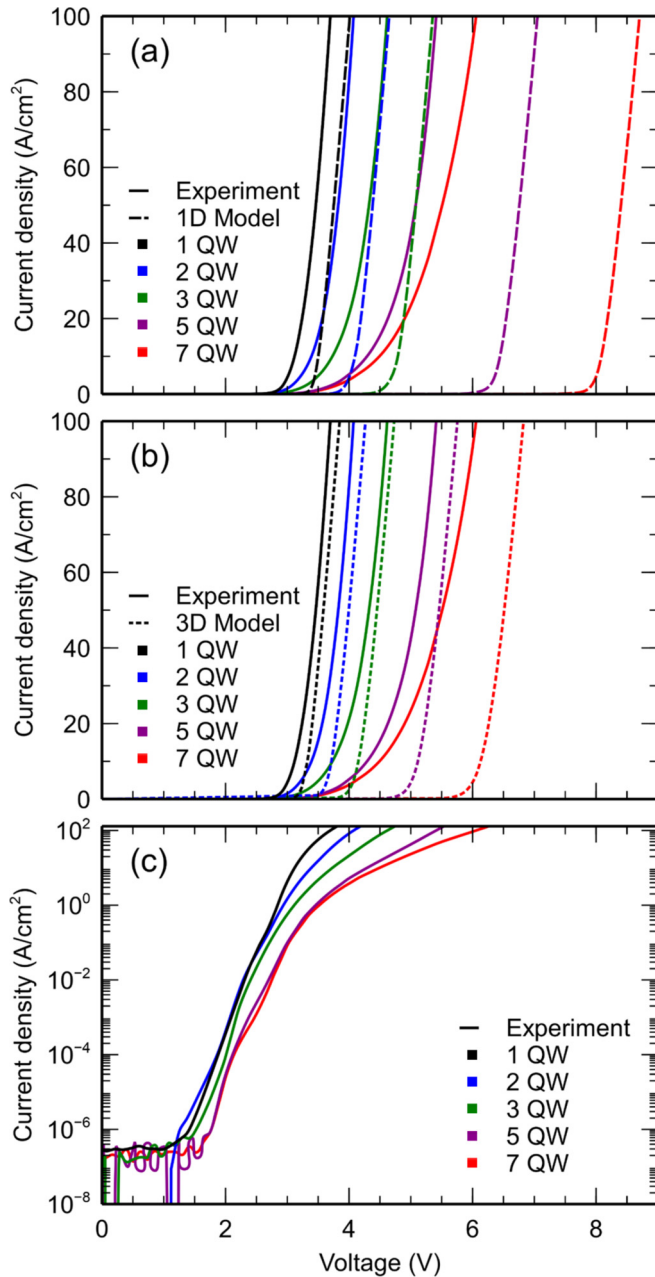
FIG. 2. (a) Experimental *J-V* curves (solid) and 1D simulated *J-V* curves (dashed) for LEDs with varying number of QWs. (b) Experimental *J-V* curves (solid) and 3D simulated *J-V* curves (dotted) for LEDs with varying number of QWs. The 1D simulations predict significantly higher forward voltage compared to their 3D counterparts. (c) Experimental *J-V* curves on a semilogarithmic scale show the low current density device behavior.

at 20 A cm^{-2} for the samples with one, two, three, five, and seven QWs are 508, 519, 515, 524, and 516 nm, respectively. All samples in this series, including the one-QW sample, showed large excess voltage relative to V_{ph}. A portion of this excess voltage is attributed to the high Al content in the AlGaN capping layers, based on previous findings [36]. Another known contribution to the voltage is the nonideal contact resistance in our samples (see [34] for further discussion and contact analysis). Calculating the specific resistivity from the

linear regime of the *J-V* curves yields 3.8×10^{-3}, 4.0×10^{-3}, 4.5×10^{-3}, 4.5×10^{-3}, $6.7 \times 10^{-3} \, \Omega \, \text{cm}^2$ for the samples with one, two, three, five, and seven QWs, respectively.

The predicted *J-V* data simulated using a 1D-DDCC algorithm are shown as dashed curves in Fig. 2(a) and the *J-V* data for 3D simulated structures are shown as dotted curves in Fig. 2(b). Both the 1D and 3D *J-V* curves were adjusted based on the average experimental specific resistivity (see [34] for details regarding this correction). Compared to 1D simulations, 3D simulations consistently predict a lower V_F and are in better agreement with experimental results. 3D simulations allow for the inclusion of in-plane alloy fluctuations, which were shown to play a key role in carrier transport for blue LEDs by providing preferential current paths for carriers and thus leading to lower turn-on voltages [4,5,37]. The same conclusion can be made for green LEDs where considering the 3D description of alloys delivers simulations with improved predictive capability. At 100 A cm^{-2} the average voltage added per QW is 0.41 V from experimental data and 0.48 V from 3D simulations.

Reasonable agreement between 3D simulations and experimental results was achieved without the need to adjust the polarization parameters, whereas in much 1D commercial software, the known polarization values [3] are reduced by as much as 50% to predict voltages consistent with experiments. Despite the improved predictive capability of the 3D simulations, discrepancies between the experimental and simulated *J-V* curves exist. In the low current density regime near diode turn-on, the shape of the *J-V* curves for the simulations and experiments deviate. The model used here is not able to capture certain physical phenomena which occur near LED turn-on. Namely, carrier tunneling and parallel shunt pathways may alter injection at low current densities and, in addition, unintentionally nucleated V-defects may provide a lower voltage barrier to carrier injection. The absence of these phenomena in our model may explain some of the differences which exist between experimental and simulation results. A semilogarithmic plot of the experimental *J-V* data is included in Fig. 2(c) to highlight the low current density device behavior.

Such a voltage penalty per QW is not measured in similar experimental or simulated MQW LED structures emitting in the blue spectral range. In previous work, a simulated $V_F = 2.9$ V at 20 A cm^{-2} was reported for a six-QW blue *c*-plane LED [5], which is close to the photon voltage ($V_{ph} = 2.76$ V at $\lambda = 450$ nm). The results presented here suggest that the voltage penalty and its increase with QW number is inherent to *c*-plane LEDs emitting in the green spectral range and longer.

To further elucidate the role of QW number on V_F, the effective band diagrams of each structure were examined. In Fig. 3(a) the average In and Al composition in the *Z* direction indicate the position of the InGaN QWs and AlGaN cap layers, respectively. The effective band diagram and V_F obtained by the 3D-DDCC solver for structures with one, three, five, and seven QWs are shown at 0 A cm^{-2} [Fig. 3(b)] and 10 A cm^{-2} [Fig. 3(c)]. The 0 eV position corresponds to the bottom of the $1/u_e$ potential on the *n*-GaN side of the LED, equal to the conduction band edge. From the experimental and 3D simulated *J-V* curves [Fig. 2(b)], LED structures with multiple QWs require significantly more forward bias than
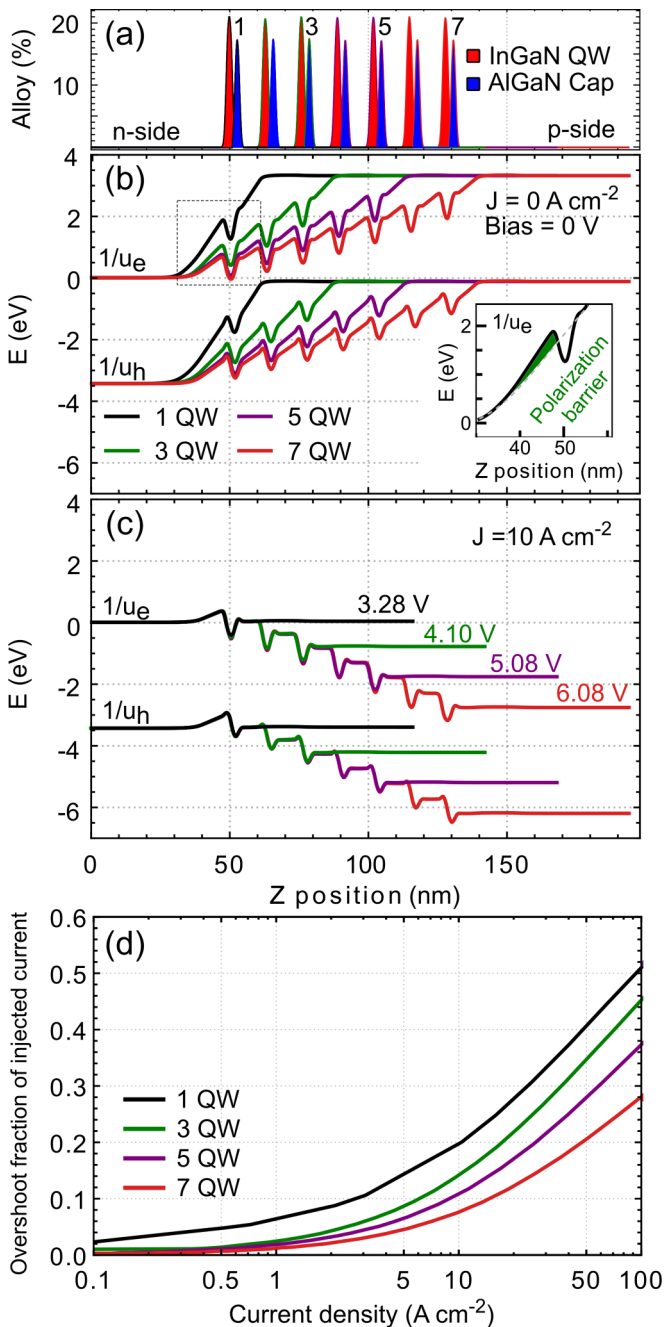
FIG. 3. (a) In and Al profiles for the InGaN QW and AlGaN cap layers in the LED active region. Effective band diagrams for LEDs with one, three, five, and seven QWs at (b) $0 \, \text{A cm}^{-2}$ and (c) $10 \, \text{A cm}^{-2}$. (d) Overshoot fraction of injected current versus current density for LEDs with one, three, five, and seven QWs.

the one-QW structure to reach the same current density. This trend is clear in the effective band diagrams where the structures with three, five, and seven QWs are beyond flat band operation at $10 \, \text{A cm}^{-2}$, further demonstrating how each additional QW results in a voltage penalty. The band structures are also consistent with the experimental data which shows that at $10 \, \text{A cm}^{-2}$ the LEDs with three, five, and seven QWs are operating at voltages above the built-in voltage of the diode V_{bi} ($\sim 3.2 \, \text{V}$). Figure 3(d) shows the simulated "overshoot," or

"escape," fraction of injected current versus current density for LEDs with varying QW number. These predictions differ from those calculated for blue LEDs [5], where overshoot only becomes significant for current densities in excess of $\sim 1 \, \text{kA cm}^{-2}$. The large overshoot current for green LEDs, relative to blue LEDs, contributes to their low PCE. Our simulated overshoot is due in part to the diode bias approaching or exceeding V_{bi} at $10 \, \text{A cm}^{-2}$. However, because the simulated voltage exceeds the experimental voltage, overflow may be overemphasized by the simulations.

Through simulation, two mechanisms that contribute to the increase of V_F with QW number have tentatively been identified. A more complete account on modeling carrier transport in green LEDs will be given elsewhere [38]. First, the polarization barriers (fixed negative polarization-related charge) appearing at the GaN/InGaN (lower barrier/QW) interfaces prevent electrons from flowing inside the QWs where they can recombine. With the fraction of indium in green emitting QWs being higher than that of blue, green LEDs will have larger polarization barriers and thus display a greater increase in V_F with the number of QWs. The second mechanism is the sequential injection of QWs and is related to the depth of the QW potential [39–41]; this effect is more pronounced in high In content QWs which have a deeper potential. The result is a penalty in voltage with larger QW number as it becomes increasingly difficult for carriers to reach the most active p-side QW [5,42].

IV. CONCLUSION

In conclusion, to understand the source of excess forward voltage in green LEDs where injection is primarily through the c-plane, we grew and fabricated LEDs by MOCVD with varying number of QWs and performed 3D simulations on the structures. We measured experimentally a systematic increase in V_F with increasing number of QWs. Simulations using the 3D-DDCC solver, which accounts for random alloy fluctuations, provided J-V trends in agreement with those obtained experimentally. The model used here does not account for carrier tunneling and the presence of shunt pathways or V-defects, which may explain discrepancies between experimental and 3D simulated J-V curves. Similar simulations in 1D significantly overestimate V_F, indicating that carrier transport cannot be accurately captured without including the 3D nature of alloy materials. We achieved reasonable agreement between 3D simulations and experimental results without adjusting the polarization parameters from their known values, indicating the improved predictive capability of the 3D-DDCC over alternative simulation methods. From these results, we propose that the polarization induced barriers at the GaN/InGaN (lower barrier/QW) interface and the sequential filling of QWs contribute significantly to the excess forward voltage in multiple quantum well c-plane green LEDs.

[1] DOE BTO SSL Program, "2018 Solid-State Lighting R&D Opportunities," https://www.energy.gov/eere/ssl/downloads/2018-solid-state-lighting-rd-opportunities.

[2] X. H. Wu, P. Fini, E. J. Tarsa, B. Heying, S. Keller, U. K. Mishra, S. P. DenBaars, and J. S. Speck, J. Cryst. Growth **189-190**, 231 (1998).

[3] F. Bernardini, V. Fiorentini, and D. Vanderbilt, Phys. Rev. B **56**, R10024 (1997).

[4] T.-J. Yang, R. Shivaraman, J. S. Speck, and Y.-R. Wu, J. Appl. Phys. **116**, 113104 (2014).

[5] C.-K. Li, M. Piccardo, L.-S. Lu, S. Mayboroda, L. Martinelli, J. Peretti, J. S. Speck, C. Weisbuch, M. Filoche, and Y.-R. Wu, Phys. Rev. B **95**, 144206 (2017).

[6] A. David, N. G. Young, C. A. Hurni, and M. D. Craven, Phys. Rev. Appl. **11**, 031001 (2019).

[7] A. M. Armstrong, M. H. Crawford, and D. D. Koleske, Appl. Phys. Express **7**, 032101 (2014).

[8] E. Kioupakis, Q. Yan, and C. G. Van de Walle, Appl. Phys. Lett. **101**, 231107 (2012).

[9] A. David and M. J. Grundmann, Appl. Phys. Lett. **97**, 033501 (2010).

[10] A notable exception to the high V's observed in green LEDs occurs when carrier injection is achieved laterally by V-defects side injection instead of vertical injection through the QW stack as in usual LEDs, such as those described here. See Ref. [11] for prediction and Ref. [12] for experimental observation.

[11] C.-K. Li, C.-K. Wu, C.-C. Hsu, L.-S. Lu, H. Li, T.-C. Lu, and Y.-R. Wu, AIP Adv. **6**, 055208 (2016).

[12] F. Jiang, J. Zhang, L. Xu, J. Ding, G. Wang, X. Wu, X. Wang, C. Mo, Z. Quan, X. Guo, C. Zheng, S. Pan, and J. Liu, Photon. Res. **7**, 144 (2019).

[13] M. Auf der Maur, A. Pecchia, G. Penazzi, W. Rodrigues, and A. Di Carlo, Phys. Rev. Lett. **116**, 027401 (2016).

[14] F. Nippert, S. Yu. Karpov, G. Callsen, B. Galler, T. Kure, C. Nenstiel, M. R. Wagner, M. Straßburg, H.-J. Lugauer, and A. Hoffmann, Appl. Phys. Lett. **109**, 161103 (2016).

[15] S. J. Chang, W. C. Lai, Y. K. Su, J. F. Chen, C. H. Liu, and U. H. Liaw, IEEE J. Sel. Top. Quantum Electron. **8**, 278 (2002).

[16] C. S. Xia, Z. M. Simon Li, Z. Q. Li, Y. Sheng, Z. H. Zhang, W. Lu, and L. W. Cheng, Appl. Phys. Lett. **100**, 263504 (2012).

[17] J.-Y. Chang, Y.-K. Kuo, and M.-C. Tsai, Phys. Status Solidi A **208**, 729 (2011).

[18] D. N. Arnold, G. David, D. Jerison, S. Mayboroda, and M. Filoche, Phys. Rev. Lett. **116**, 056602 (2016).

[19] M. Filoche, M. Piccardo, Y.-R. Wu, C.-K. Li, C. Weisbuch, and S. Mayboroda, Phys. Rev. B **95**, 144204 (2017).

[20] D. A. Browne, B. Mazumder, Y.-R. Wu, and J. S. Speck, J. Appl. Phys. **117**, 185703 (2015).

[21] Y.-L. Hu, R. M. Farrell, C. J. Neufeld, M. Iza, S. C. Cruz, N. Pfaff, D. Simeonov, S. Keller, S. Nakamura, S. P. DenBaars, U. K. Mishra, and J. S. Speck, Appl. Phys. Lett. **100**, 161101 (2012).

[22] A. I. Alhassan, R. M. Farrell, B. Saifaddin, A. Mughal, F. Wu, S. P. DenBaars, S. Nakamura, and J. S. Speck, Opt. Express **24**, 17868 (2016).

[23] A. I. Alhassan, N. G. Young, R. M. Farrell, C. Pynn, F. Wu, A. Y. Alyamani, S. Nakamura, S. P. DenBaars, and J. S. Speck, Opt. Express **26**, 5591 (2018).

[24] M. Khoury, H. Li, B. Bonef, L. Y. Kuritzky, A. J. Mughal, S. Nakamura, J. S. Speck, and S. P. DenBaars, Appl. Phys. Express **11**, 036501 (2018).

[25] B. Bonef, M. Catalano, C. Lund, S. P. Denbaars, S. Nakamura, U. K. Mishra, M. J. Kim, and S. Keller, Appl. Phys. Lett. **110**, 143101 (2017).

[26] H. Li, M. Khoury, B. Bonef, A. I. Alhassan, A. J. Mughal, E. Azimah, M. E. A. Samsudin, P. De Mierry, S. Nakamura, J. S. Speck, and S. P. DenBaars, ACS Appl. Mater. Interfaces **9**, 36417 (2017).

[27] F. Tang, M. P. Moody, T. L. Martin, P. A. J. Bagot, M. J. Kappers, and R. A. Oliver, Microsc. Microanal. **21**, 544 (2015).

[28] L. Rigutti, B. Bonef, J. Speck, F. Tang, and R. A. Oliver, Scr. Mater. **148**, 75 (2018).

[29] M. P. Moody, L. T. Stephenson, A. V. Ceguerra, and S. P. Ringer, Microsc. Res. Tech. **71**, 542 (2008).

[30] F. Tang, T. Zhu, F. Oehler, W. Y. Fu, J. T. Griffiths, F. C.-P. Massabuau, M. J. Kappers, T. L. Martin, P.A.J. Bagot, M. P. Moody, and R. A. Oliver, Appl. Phys. Lett. **106**, 072104 (2015).

[31] M. J. Galtrey, R. A. Oliver, M. J. Kappers, C. J. Humphreys, D. J. Stokes, P. H. Clifton, and A. Cerezo, Appl. Phys. Lett. **90**, 061903 (2007).

[32] M. Piccardo, C.-K. Li, Y.-R. Wu, J. S. Speck, B. Bonef, R. M. Farrell, M. Filoche, L. Martinelli, J. Peretti, and C. Weisbuch, Phys. Rev. B **95**, 144205 (2017).

[33] http://yrwu-wk.ee.ntu.edu.tw/index.php/webpi/.

[34] See Supplemental Material at http://link.aps.org/supplemental/10.1103/PhysRevMaterials.4.054604 for a description of the method and parameters used in the computations as well as the device contact and specific resistivity analysis.

[35] C. Geuzaine and J.-F. Remacle, Int. J. Numer. Methods Eng. **79**, 1309 (2009).

[36] T. Shioda, H. Yoshida, K. Tachibana, N. Sugiyama, and S. Nunoue, Phys. Status Solidi A **209**, 473 (2012).

[37] Y.-R. Wu, R. Shivaraman, K.-C. Wang, and J. S. Speck, Appl. Phys. Lett. **101**, 083505 (2012).

[38] G. Lheureux, C. Lynsky, B. Bonef, Y.-R. Wu, C. Weisbuch, and J.S. Speck (unpublished).

[39] H. Schneider and K. v. Klitzing, Phys. Rev. B **38**, 6160 (1988).

[40] K. Fröjdh, S. Marcinkevičius, U. Olin, C. Silfvenius, B. Stålnacke, and G. Landgren, Appl. Phys. Lett. **69**, 3695 (1996).

[41] S. Marcinkevičius, R. Yapparov, L. Y. Kuritzky, Y.-R. Wu, S. Nakamura, S. P. DenBaars, and J. S. Speck, Appl. Phys. Lett. **114**, 151103 (2019).

[42] A. David, M. J. Grundmann, J. F. Kaeding, N. F. Gardner, T. G. Mihopoulos, and M. R. Krames, Appl. Phys. Lett. **92**, 053502 (2008).